Supporting Information for

Sulfur-dissolved high-entropy alloys with ultrawide-bandwidth electromagnetic-wave absorption properties synthesized via mechanochemical process

Jiawen Hu[a], Linwen Jiang[a, *], Hang Liu[a], Jiawei Jin[a], Lei Jia[a], Anhua Wu[b], Xiaofeng Zhang[c, *]

[a]School of Materials Science and Chemical Engineering, State Key Laboratory Base of Novel Functional Materials and Preparation Science, Ningbo University, Ningbo 315211, PR China

[b]Shanghai Institute of Ceramics, Chinese Academy of Sciences, Shanghai 201800, PR China

[c]Institute of New Materials, Guangdong Academy of Science, National Engineering Laboratory for Modern Materials Surface Engineering Technology, Guangzhou 510651, PR China

[*] Corresponding author.

Corresponding author.
E-mail addresses: jianglinwen@nbu.edu.cn (Linwen Jiang), zhangxiaofeng@gdinm.com (Xiaofeng Zhang).

The corrosion resistance test conditions and sample preparation process

The corrosion resistance test conditions and sample preparation process in Fig. 5 (a-c) are as follows:

(1) An electrochemical workstation (CHI760E) is used to test the potentiodynamic polarization curve and electrochemical impedance spectra (EIS) in the 3.5 wt.% NaCl solution. The electrochemical tests adopt a three-electrode system. A sample-loaded carbon paper is used for the working electrode, and a platinum metal sheet and saturated calomel electrode (SCE) are used as auxiliary and reference electrodes, respectively. The open-circuit potential of samples is obtained after being soaked for 1800 s. The potentiodynamic polarization curves are measured at a scanning rate of 0.5 mV/s. Corrosion potential and corrosion current density are obtained from polarization curves. The EIS test is carried out with a scan amplitude of 5 mV and a frequency range of 100 kHz - 0.1 Hz.

(2) The samples were prepared as follows: first, 5 mg of sample powder, 120 μL of naphthol, 200 μL of isopropanol and 600 μL of deionized water were uniformly mixed. Subsequently, 35 μL of the mixed solution was added dropwise onto a carbon paper with size of 0.5 × 0.5 cm^2. Finally, these samples were dried at 60 °C for 10 minutes.

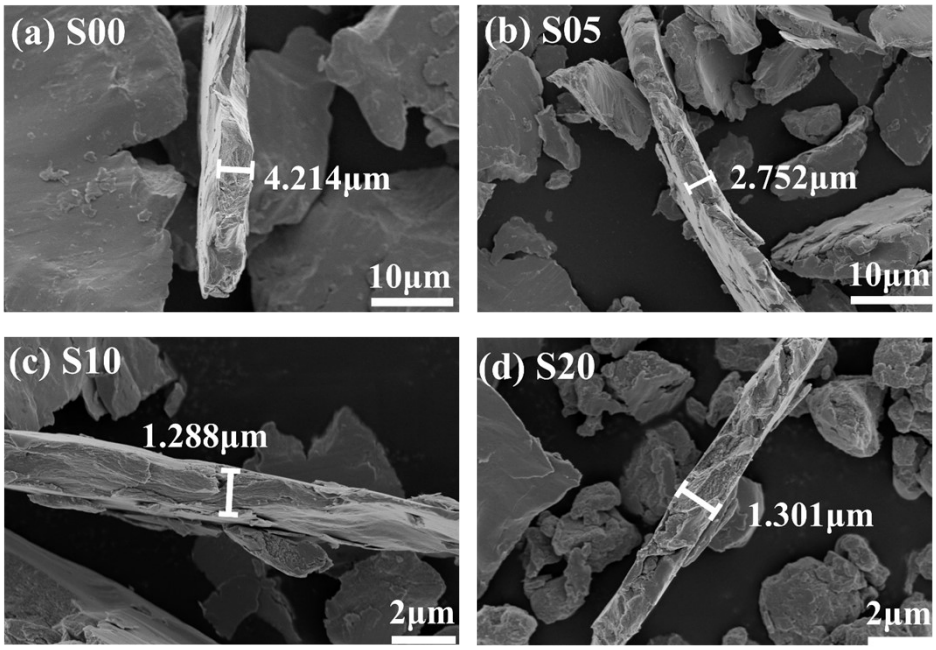

Fig. S1. The thickness images of (a) S00, (b) S05, (c) S10 and (d) S20.

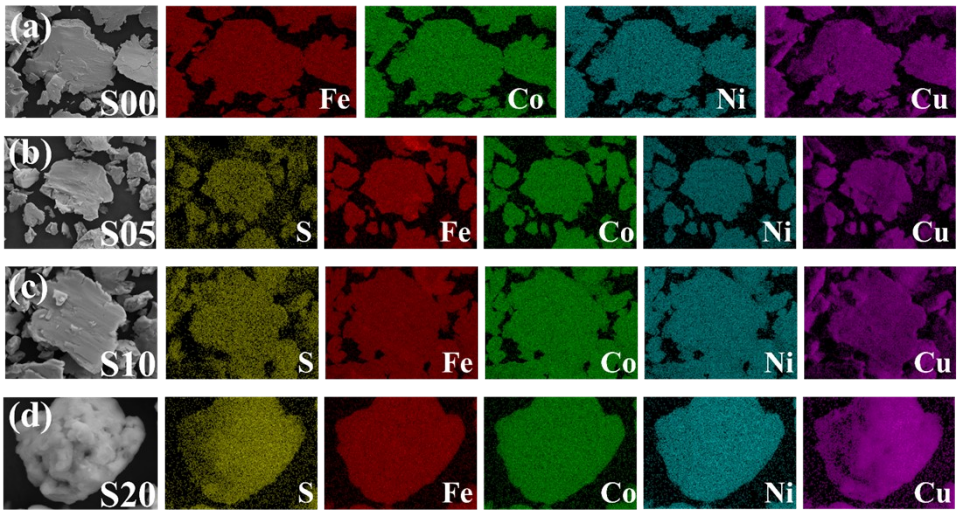

Fig. S2. EDS element mapping images of (a) S00, (b) S05, (c) S10 and (d) S20.

Table S1. Melting point, crystal structure, atomic radius and Pauling electronegativity of raw materials.

Element	Fe	Co	Ni	Cu	S
Melting point(°C)	1538	1495	1455	1084.6	115.21
Crystal structure	BCC	HCP	FCC	FCC	FCO
Atomic radius (pm)	126	125	124	128	88
Pauling electronegativity	1.83	1.88	1.91	1.90	2.58

Table S2. Electrochemical parameters of equivalent circuit under different stray current density.

Samples	R_s	Q-Yo	Q-n	R_{ct1}	CPE	R_{ct2}
S00	1.983	0.0005664	0.8913	16.18	0.00035766	3402
S05	3.324	0.00061789	0.72983	55.21	0.00031103	5069
S10	2.866	0.0026577	0.63878	18.83	0.00061179	3295
S20	2.925	0.0010336	0.65015	23.87	0.00059115	5105

Table S3. Comparison of corrosion-resistance performances of different HEAs.[1-5]

Samples	Solution	I_{corr} ($\mu A/cm^2$)	E_{corr} (mV)	Ref.
FeCoNiCu	3.5 wt.% NaCl	5.04	-0.364	Ref. 1
FeCoNiCu	3.5 wt.% NaCl	5.78	-0.43	Ref. 2
$FeCoNiCuAlCe_{0.01}$	3.5 wt.% NaCl	5.27	-0.43	Ref. 2
$FeCoNiCuAlCe_{0.03}$	3.5 wt.% NaCl	4.61	-0.43	Ref. 2
$FeCoNiCuAlCe_{0.09}$	3.5 wt.% NaCl	4.01	-0.45	Ref. 2
$FeCoNiAl_{0.3}$	3.5 wt.% NaCl	5.02	-0.204	Ref. 3
FeCoNiCrBSiNb	3.5 wt.% NaCl	5.20	-0.390	Ref. 4
$Ti_{21.6}Al_{11.3}Cr_{19.4}Si_{23.5}V_{22.0}O_{2.2}$	3.5 wt.% NaCl	6.14	-0.541	Ref. 4
FeCoNiCr	3.5 wt.% NaCl	2.51	-0.036	Ref. 5
S05	3.5 wt.% NaCl	1.40	132.33	This work

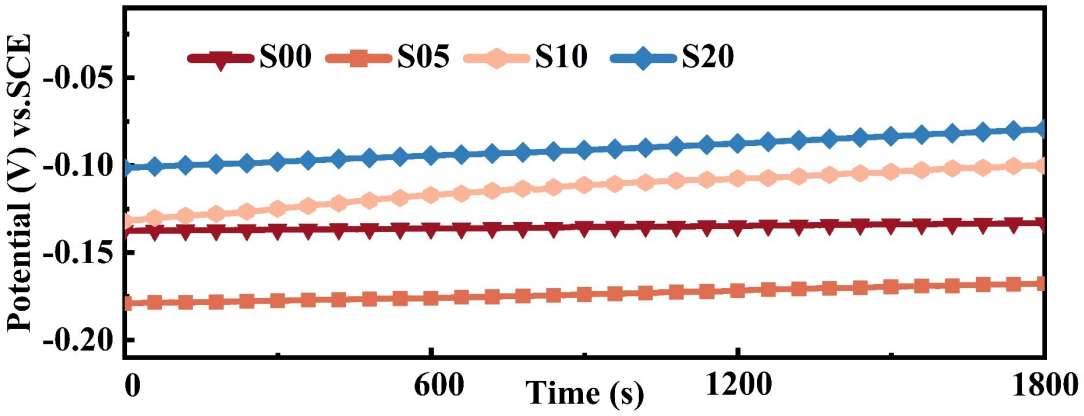

Fig. S3. Open-circuit potentials of $FeCoNiCuS_x$ (x=0, 0.05, 0.10, 0.20) HEAs.

Specifically, the dielectric loss can be expressed with the Debye equation as follows:

$$\varepsilon_r = \varepsilon' - j\varepsilon'' = \varepsilon_\infty + \frac{\varepsilon_s - \varepsilon_\infty}{1 + j2\pi f\tau} \quad (1)$$

$$\varepsilon' = \varepsilon_\infty + \frac{\varepsilon_s - \varepsilon_\infty}{1 + (2\pi f)^2\tau^2} \quad (2)$$

$$\varepsilon'' = \varepsilon_P + \varepsilon_C = \frac{(\varepsilon_s - \varepsilon_\infty)2\pi f\tau}{1 + (2\pi f)^2\tau^2} + \frac{\sigma}{2\pi f\varepsilon_0} \quad (3)$$

where ε_s is the static dielectric constant and ε_∞ is the dielectric constant of infinite frequency and τ is the relaxation time, σ is the conductivity, and ε_p and ε_c is the polarization loss and the conductivity loss, respectively. The dielectric losses result from polarization losses caused by the establishment of polarization and conductivity losses caused by carrier transfer. To further investigate the mechanism of dielectric losses in materials, we did the following derivations. The equation S1 can be obtained if there are no conductivity losses, and equation S2 is derived from equation S3 using equation 2.

$$\varepsilon'' = \varepsilon_P + \frac{(\varepsilon_s - \varepsilon_\infty)2\pi f\tau}{1 + (2\pi f)^2\tau^2} \quad (S1)$$

$$\frac{\varepsilon''}{f} = 2\pi\tau\varepsilon' - 2\pi\tau\varepsilon_\infty \quad (S2)$$

$$\varepsilon'' = \varepsilon_C = \frac{\sigma}{2\pi f\varepsilon_0} \quad (S3)$$

Because τ and ε_∞ are constants, plotting ε''/f and ε' will give a straight line when there is no conductivity loss. In other words, when the ε''/f-ε' plots is straight, there is no conductivity loss occurring. Secondly, equation 3 is converted into equation S3 assuming no polarization loss. Because σ is a constant, the ε''-f^{-1} plot will be a straight line when there is no polarization loss. In other words, when the ε''-f^{-1} plots is straight, there is no polarization loss occurring.

The reflection loss (RL) at varying thicknesses of the samples were shown in Fig. S4. With the increase of S content in HEAs, the samples demonstrated significantly enhanced RL capabilities, particularly at low-frequency. As shown in Fig.S4(a), the optimum RL of S00 was -38.8 dB at 18 GHz, and as the S content of the high-entropy alloys increased in Fig.S4(d), the optimum RL of S20 was -55.4 dB at 6.52 GHz (C-band). Therefore, the solid solution effect of S strengthened the electromagnetic-wave absorbing performance of high-entropy alloys, which was favorable for high-entropy alloys wave-absorbing materials to achieve the low-frequency ultra-broadband absorption performances.

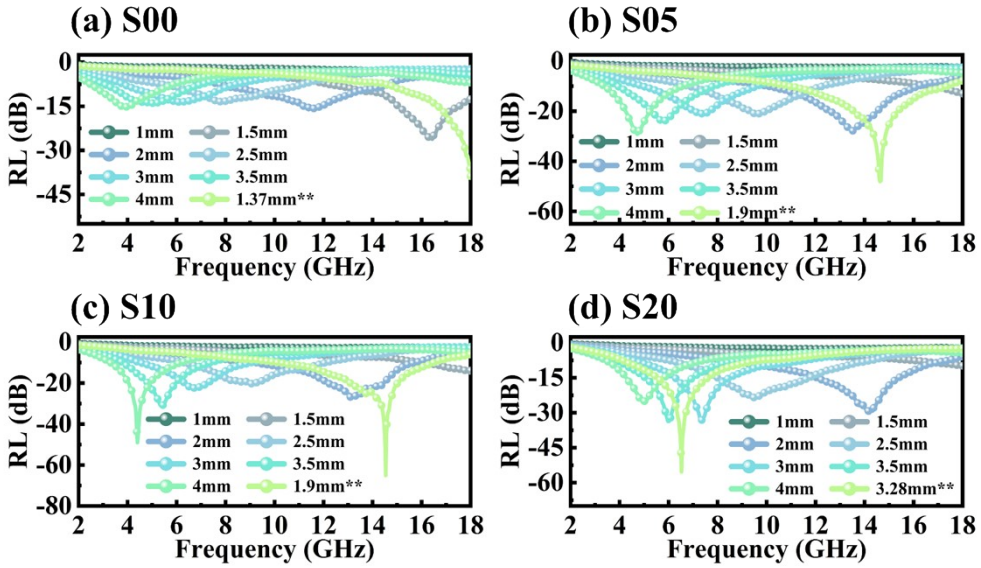

Fig. S4. (a-e) The 2D RL curves at different thicknesses of $FeCoNiCuS_x$ (x=0, 0.05, 0.10, 0.20) HEAs.

Table S4. The comparison of RL performances of all samples in this work.

Samples	RL_{min} (dB)	Frequency (GHz)	Thickness (mm)
S00	-38.8	18.00	1.37
S05	-48.2	14.62	1.90
S10	-65.2	14.53	1.90
S20	-55.4	6.52	3.28

The radar chart provided a comprehensive performance evaluation of the relevant EMA materials[5-11] to explore the unique advantages of $FeCoNiCuS_x$ HEAs, as shown in Fig. S5. Detailed values were given in Table S5 of supporting information. Compared with the properties of C-dissolved HEAs, B-dissolved HEAs and other EMA materials, it was found that S10 and S20 achieved strong RL and ultra-wide EAB, while the thickness was thinner than most EMA materials. In addition, S10 and S20 also had better corrosion resistance than these C-dissolved HEAs, B-dissolved HEAs. Overall, $FeCoNiCuS_x$ HEAs demonstrated excellent comprehensive performances, indicating that the obtained products as EMA materials were efficient and durable with great potential for applications in harsh environments.

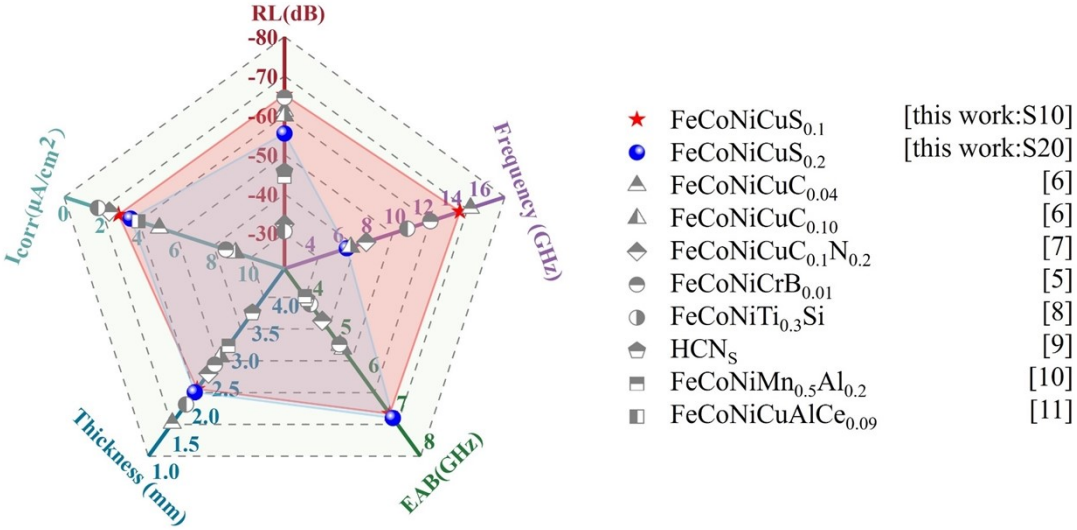

Fig. S5. Radar chart of comprehensive performances for different EMA materials.

Table S5. The comparison of comprehensive properties with related materials.

Samples	RL (dB)	F (GHz)	EAB (GHz)	T (mm)	I_{corr} (μA/cm²)	Ref.
S10	-65.2	14.53	6.89	2.22	2.93	This work
S20	-55.4	6.52	7	2.16	3.59	This work
$FeCoNiCuC_{0.04}$	-61.1	15.28	5.1	1.6	5.14	Ref.6
$FeCoNiCuC_{0.10}$	-59.9	6.78	5.2	2.8	9.25	Ref.6
$FeCoNiCuC_{0.1}N_{0.2}$	-32.3	7.89	4.46	2.5	2.43	Ref.7
$FeCoNiCrB_{0.01}$	-64.5	12.43	5.08	2.66	8.729	Ref.5
$FeCoNiTi_{0.3}Si$	-30.5	10.8	4.03	1.94	1.82	Ref.8
HCN_S	-45.7	-	3.9	3.6	-	Ref.9
$FeCoNiMn_{0.5}Al_{0.2}$	-44.4	-	3.825	3	-	Ref.10
$FeCoNiCuAlCe_{0.09}$	-	-	-	-	4.01	Ref.11

The Laser Particle Size Analysis (LPSA) test

The particle size of each sample was analyzed using the LPSA test, and the results are shown in Fig. S6. The average particle size of the samples gradually decreased from 17.20 μm (S00) to 2.61 μm (S20), which is consistent with the results of the particle size distribution graph in Fig. 3.

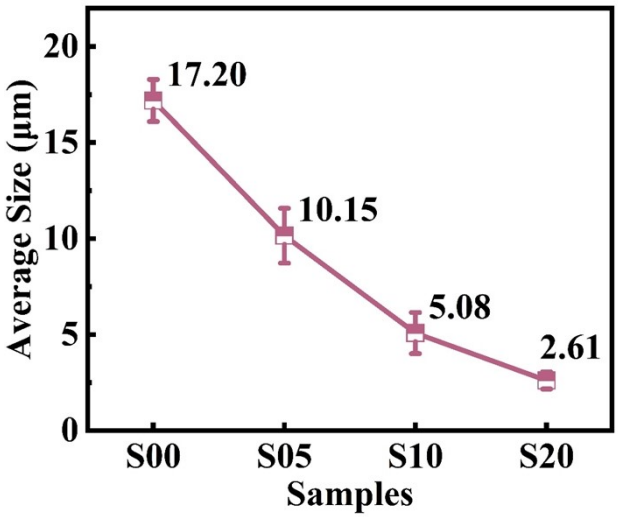

Fig. S6. The average sizes of all samples (S00, S05, S10 and S20) measured by LPSA.

Meanwhile, the degree of lattice distortion was analyzed, which can be reflected by the strain within the $FeCoNiCuS_x$ HEAs. When small-sized S atoms were introduced into the HEAs, it would lead to lattice distortion. The presence of S atoms in the lattice interstitials cause the increase of the lattice parameters, which in turn enhanced the strain in the HEAs. Therefore, as shown in Fig. S7, the strain increased from 0.781 (S00) to 1.264 (S20) with the increase of S in the HEAs.

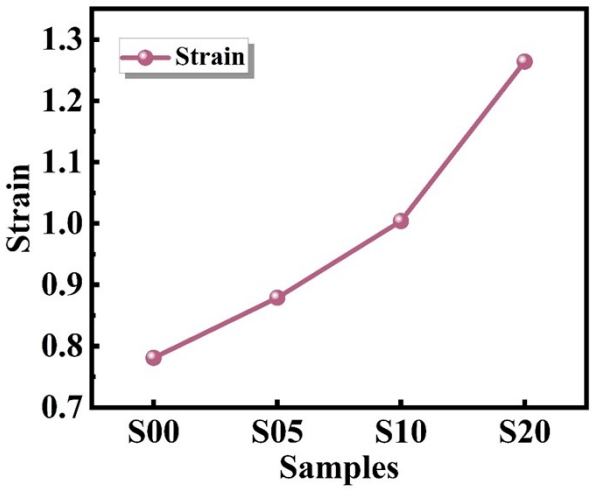

Fig. S7. The strain of all samples (S00, S05, S10 and S20).

References

1 Z. Wu, B. Li, M. Chen, Y. Yang, R. Zheng, L. Yuan, Z. Li, X. Tan and H. Xu, *J. Alloys Compd.*, 2022, **901**, 163665.

2 X. Yan, H. Guo, W. Yang, S. Pang, Q. Wang, Y. Liu, P. K. Liaw and T. Zhang, *J. Alloys Compd.*, 2021, **860**, 158436.

3 H. Zhang, W. Li, H. Xu, L. Chen, J. Zeng, Z. Ding, W. Guo and B. Liu, *Coatings*, 2022, **12**, 628.

4 Y.-A. Shen, H.-M. Hsieh, S.-H. Chen, J. Li, S.-W. Chen and H. Nishikawa, *Appl. Surf. Sci.*, 2021, **546**, 148931.

5 H. Zhou, L. Jiang, L. Jia, S. Zhu, L. Wang, A. Wu and X. Zhang, *J. Alloys Compd.*, 2023, **959**, 170579.

6 J. Yang, L. Jiang, Z. Liu, Z. Tang and A. Wu, *J. Mater. Sci. Technol.*, 2022, **113**, 61-70.

7 L. Jia, L. Jiang, J. Hu, J. Jin, S. Yan, A. Wu and X. Zhang, *Acs Appl. Mater. Inter.*, 2023, **15**, 58651-58662.

8 L. Jia, L. Jiang, H. Zhou, S. Yan, A. Wu and X. Zhang, *Phys. Chem. Chem. Phys.*, 2023, **25**, 22011-22021.

9 Q. Ban, Y. Li, L. Li, Y. Qin, Y. Zheng, H. Liu and J. Kong, *Carbon*, 2023, **201**, 1011-1024.

10 H. Pang, Y. Duan, M. Gao, L. Huang, X. Liu and Z. Li, *Mater. Today Nano*, 2022, **20**, 100243.

11 Z. Wu, B. Li, M. Chen, Y. Yang, R. Zheng, L. Yuan, Z. Li, X. Tan and H. Xu, *J. Alloys Compd.*, 2022, **901**, 163665.